UNIVERSITY
OF TRENTO

DIPARTIMENTO DI INGEGNERIA E SCIENZA DELL'INFORMAZIONE

38123 Povo – Trento (Italy), Via Sommarive 14
http://www.disi.unitn.it

MULTI-RESOLUTIONRETRIEVAL OF NON-MEASURABLE
EQUIVALENT CURRENTS IN MICROWAVE IMAGING
PROBLEMS - EXPERIMENTAL ASSESSMENT

P. Rocca

January 2011

Technical Report # DISI-11-037

Multi-resolution Retrieval of Non-measurable Equivalent Currents in Microwave Imaging Problems - Experimental Assessment

Paolo Rocca

Electromagnetic Diagnostic Laboratory, ELEDIALab

Department of Information Engineering and Computer Science

University of Trento, Via Sommarive 14, 38050 Trento - Italy

Tel. +39 0461 882057, Fax +39 0461 882093

E-mail: *paolo.rocca@disi.unitn.it*

Multi-resolution Retrieval of Non-measurable Equivalent Currents in Microwave Imaging Problems - Experimental Assessment

Paolo Rocca

Abstract

In this paper, an approach based on a multi-scaling strategy for the reconstruction of the non-measurable components of equivalent current distributions is tested against experimental data. An extensive set of simulations is carried out considering single and multiple scatterers with homogeneous as well as inhomogeneous properties. Selected results are reported and discussed to show potentialities and limitations of the method.

Key words: Microwave imaging, inverse scattering, multi-scaling strategy, non-measurable currents.

1 Introduction

The retrieval of unknown targets embedded in inaccessible regions is a problem still actual and of interest [1] that need the development of efficient and reliable procedures for their application to real world problems [2][3]. Many strategies in microwave imaging reformulate the arising inverse scattering problem as the solution of an equivalent inverse source problem to determine either the profiles [4] or the dielectric properties [5][6][7] of unknown objects embedded in an inaccessible region. Despite the linearity of the inverse source problem with respect to the unknown equivalent current density within the investigation domain [8][9][10], the problem still remains ill-posed in the sense of Hadamard [11]. As a matter of fact, the presence of non-radiating, or non-measurable contributions, causes the non-uniqueness of the equivalent source [12][13]. As regards the null space in source type integral equations, several theoretical studies have been reported in the scientific literature [14][15][16]. However, only a few techniques have been proposed [6][7] to recover the contribute of the non-measurable currents from measured field data. The lack of information on these components results in too inaccurate reconstructions that generally suffer from a strong low-pass effect [5][17]. Since the achievable spatial resolution is strictly related to the number of basis functions modeling the unknowns, the higher is the spatial resolution the greater is the number of basis functions required to obtain accurate reconstructions. Consequently, the dimension of the null space turns out to be very large [14] due to the band-limited nature of the scattered field [18]. Moreover, the number of local minima grows, severely affecting the potentialities of the inversion procedures.

In order to avoid these drawbacks, an iterative multi-resolution method for the reconstruction of the non-measurable components of the equivalent current density has been recently presented in [19]. The key features of the approach, called Iterative Multi-Scaling Approach for Non-Radiating currents ($IMSA - NR$), are the ability to reduce the dimension of the kernel space of the scattering operator and to improve the accuracy of the reconstruction. In this work, the $IMSA - NR$ is further assessed by considering experimental data acquired in a laboratory controlled environment.

The outline of the paper is as follows. The inverse scattering problem is mathematically formulated in Sect. 2 where the multi-resolution procedure is briefly summarized, as well. A

representative set of results is shown in Sect. 3 to assess the effectiveness of the $IMSA - NR$ when dealing with experimental data. Eventually, some conclusions are drawn and possible developments are discussed (Sect. 4).

2 Mathematical Formulation

Let us consider a $2D$ microwave imaging system where a set of V known probing source generating TM-polarized fields (called *incident fields*), $E_{inc}^v(x,y) = E_{inc}^v(x,y)\,\hat{z}$, $v = 1, \ldots, V$, illuminates an investigation domain Γ_{inv}. The *scattered fields*, $E_{scat}^v(x,y)$, $v = 1, \ldots, V$, are collected on a set of $M^{(v)}$ electromagnetic sensors located in an external observation domain Γ_{obs}. The $IMSA$ presented in [20] considers a succession of $s = 1, ..., S$ steps aimed at enhancing the reconstruction accuracy within a Region-of-Interest (RoI) belonging to Γ_{inv} where the scatterer is supposed to be located. With reference to the s-th step of the multi-scaling procedure, the unknown contrast function, $\tau(x,y)$, and equivalent current densities, $J_{eq}^v(x,y)$, $v = 1, ..., V$, are represented through a linear combination of rectangular basis functions ($\Omega_{n(i)}(x,y)$ and $\Upsilon_{n(i)}(x,y)$, respectively) having different resolution such that

$$\tau(x,y) = \sum_{i=1}^{I} \sum_{n(i)=1}^{N(i)} \tau\left(x_{n(i)}, y_{n(i)}\right) \Omega_{n(i)}(x,y) \, , \quad I = s \tag{1}$$

$$J_{eq}^v(x,y) = \sum_{i=1}^{I} \sum_{n(i)=1}^{N(i)} J_{eq}^v\left(x_{n(i)}, y_{n(i)}\right) \Upsilon_{n(i)}(x,y) \, , \quad I = s \tag{2}$$

where the index i represents the spatial resolution level, $i = 1, ..., I$, $I = s$ being the finer resolution and $N(i)$ is the number of partition sub-domains at the i-th resolution level.

To solve the inverse problem at hand, the *Data* and *State* equations are evaluated at each step of the multi-resolution approach within the RoI where a synthetic zoom takes place [21] and the dielectric properties of the remaining part of Γ_{inv} are set to those of the background. More specifically, the Lippmann-Schwinger integral equations [22] are expressed as

$$E_{scat}^v(x_m, y_m) = \sum_{n(i)=1}^{N(i)} J_{eq}^v\left(x_{n(i)}, y_{n(i)}\right) G_{2d}^{ext,v}\left(A_{n(i)}, \rho_{n(i),m}\right) \tag{3}$$

$$\forall (x_m, y_m) \in \Gamma_{obs} \, ; \, m = 1, \ldots, M^{(v)} \, ; \, v = 1, \ldots, V$$

4

with $i = I = s$ and

$$\tau\left(x_{n(i)}, y_{n(i)}\right) E_{inc}^{v}\left(x_{n(i)}, y_{n(i)}\right) = J_{eq}^{v}\left(x_{n(i)}, y_{n(i)}\right) - \tau\left(x_{n(i)}, y_{n(i)}\right)$$

$$\left\{ \sum_{u(i)=1}^{N(i)} J_{eq}^{v}\left(x_{u(i)}, y_{u(i)}\right) G_{2d}^{int,v}\left(A_{u(i)}, \rho_{u(i),n(i)}\right) \right\} \quad (4)$$

$$\forall\left(x_{n(i)}, y_{n(i)}\right) \in \Gamma_{inv} \, ; \, v = 1, \dots, V$$

where the unknown contrast function is defined as

$$\tau\left(x, y\right) = \frac{\widetilde{\varepsilon}(x,y)}{\varepsilon_0} - 1 \, , \quad (5)$$

$\widetilde{\varepsilon}\left(x, y\right) = \varepsilon_0 \left\{ \varepsilon_R\left(x, y\right) - j\frac{\sigma(x,y)}{\omega\varepsilon_0} \right\}$ being the complex permittivity. Moreover, ε_R and σ are the relative permittivity and conductivity, respectively, and ε_0 is the permittivity of the free-space. In (3) and (4), $G_{2d}^{ext,v}$ and $G_{2d}^{int,v}$ denote the discretized Green's operators [20]. Moreover, $A_{n(i)}$ (or $A_{u(i)}$) is the area of the n-th (or u-th) cell at the i-th resolution level, $\rho_{n(i),m} = \sqrt{\left(x_{n(i)} - x_m\right)^2 + \left(y_{n(i)} - y_m\right)^2}$ and $\rho_{u(i),n(i)} = \sqrt{\left(x_{u(i)} - x_{n(i)}\right)^2 + \left(y_{u(i)} - y_{n(i)}\right)^2}$.

It is well known [6] that the equivalent current densities $J_{eq}^{v}\left(x, y\right)$ can be expressed through the linear combination of two different contributions

$$J_{eq}^{v}\left(x, y\right) = \sum_{i=1}^{I} \left\{ \sum_{n(i)=1}^{R(i)} \theta_{n(i)}^{v} \Theta_{n(i)}^{v}\left(x, y\right) + \sum_{n(i)=R(i)+1}^{N(i)} \phi_{n(i)}^{v} \Phi_{n(i)}^{v}\left(x, y\right) \right\} \quad (6)$$

namely the *minimum norm* (MN) or radiating current density and the *non-measurable* (NR) current density where in (2) it is $\left\{ J_{eq}^{v}\left(x_{n(i)}, y_{n(i)}\right) \right\} = \left\{ \theta_{n(i)}^{v} \right\} \cup \left\{ \phi_{n(i)}^{v} \right\}$ and $\left\{ \Upsilon_{n(i)}\left(x, y\right) \right\} = \left\{ \Theta_{n(i)}^{v}\left(x, y\right) \right\} \cup \left\{ \Phi_{n(i)}^{v}\left(x, y\right) \right\}$. The MN components of the equivalent source generate the scattered fields in the observation domain Γ_{obs}. Their coefficients, $\theta_{n(i)}^{v}$, can be defined at each step of the multi-resolution procedure through a Singular Value Decomposition (SVD) of the Green's operator by solving Eq. (3). More in detail and according to the guidelines in [7], these coefficients are given by

$$\theta_{n(i)}^{v} = \frac{1}{\xi_{n(i)}^{v}} \left\{ \sum_{m=1}^{M^{(v)}} \left[U_m^{v}\left(x, y\right) \right]^{*} E_{scat}^{v}\left(x_m, y_m\right) \right\} \, , \, n(i) = 1, \dots, R(i) \quad (7)$$

where $\xi_{n(i)}^{v}$, $n(i) = 1, \dots, R(i)$, is the set of non trivial singular values, $R(i)$ being the rank of the Green's operator, and $\{ U_m^{v}\left(x, y\right) \}$ is an orthonormal system of eigenvectors obtained from the SVD. The basis functions $\left\{ \Theta_{n(i)}^{v}\left(x, y\right) \right\}$, $n(i) = 1, ..., R(i)$, and $\left\{ \Phi_{n(i)}^{v}\left(x, y\right) \right\}$, $n(i) =$

$R(i) + 1, ..., N(i)$, used in (6) are two sets of orthogonal eigenvectors still defined through the SVD [7].

In order to compute the non-radiating coefficients, $\phi_{n(i)}^v$, $n(i) = R(i) + 1, ..., N(i)$, as well as the coefficients of the contrast function, $\tau\left(x_{n(i)}, y_{n(i)}\right)$, $n(i) = 1, ..., N(i)$, the following cost functional, $\Psi^{(s)} = \frac{\Omega^{(s)}}{C^{(s)}}$, is minimized at each step of the multi-resolution procedure where

$$
\begin{aligned}
\Omega^{(s)} = & \sum_{v=1}^{V} \sum_{j=1}^{I} \sum_{n(j)=1}^{N(j)} \left\{ w\left(x_{n(j)}, y_{n(j)}\right) \left| \tau\left(x_{n(j)}, y_{n(j)}\right) E_{inc}^v\left(x_{n(j)}, y_{n(j)}\right) + \right. \right. \\
& - \left[\sum_{t(j)=1}^{R(j)} \theta_{t(j)}^v \Theta_{t(j)}^v\left(x_{n(j)}, y_{n(j)}\right) + \sum_{t(j)=R(j)+1}^{N(j)} \phi_{t(j)}^v \Phi_{t(j)}^v\left(x_{n(j)}, y_{n(j)}\right) \right] + \\
& + \tau\left(x_{n(j)}, y_{n(j)}\right) \sum_{u(j)=1}^{N(j)} \left[\sum_{t(j)=1}^{R(j)} \theta_{t(j)}^v \Theta_{t(j)}^v\left(x_{u(j)}, y_{u(j)}\right) + \right. \\
& \left. \left. + \sum_{t(j)=R(j)+1}^{N(j)} \phi_{t(j)}^v \Phi_{t(j)}^v\left(x_{u(j)}, y_{u(j)}\right) \right] G_{2d}^v\left(A_{u(j)}, \rho_{u(j),n(j)}\right) \right|^2 \right\}
\end{aligned}
\tag{8}
$$

and $C^{(s)}$ is the normalization coefficient

$$
C^{(s)} = \sum_{v=1}^{V} \sum_{j=1}^{I} \sum_{n(j)=1}^{R(j)} \left\{ w\left(x_{n(j)}, y_{n(j)}\right) \left| \theta_{t(j)}^v \Theta_{t(j)}^v\left(x_{n(j)}, y_{n(j)}\right) \right|^2 \right\} .
\tag{9}
$$

Moreover, w is a weighting function defined as

$$
w\left(x_{n(j)}, y_{n(j)}\right) = \begin{cases} 0 & if \left(x_{n(j)}, y_{n(j)}\right) \notin RoI \\ 1 & if \left(x_{n(j)}, y_{n(j)}\right) \in RoI \end{cases}
\tag{10}
$$

The multi-step process stops ($s = S_{end}$) when a stationary condition based on the analysis of qualitative reconstruction parameters [19] is achieved. To minimize the functional $\Psi^{(s)}$, a well assessed conjugate gradient approach based on an alternate minimization strategy [23] is considered.

3   Experimental Validation

In this section, numerical results concerned with the inversion of experimental aspect-limited data as reported and analyzed. The first part of this section deals with the reconstruction of homogeneous lossless as well as lossy dielectric targets [24]. The reconstruction of inhomogeneous objects [25] is discussed in the second part. The scattering data have been made available

thank to the courtesy of the Institute Fresnel, Marseille, France. A thoroughly description of the experimental setup can be found in [24] and [25].

In order to quantify the effectiveness of the proposed approach and to compare with the single step (*bare*) procedure [7], the *location error*, δ, and the *occupation area error*, Δ, are defined as

$$\delta = \frac{\sqrt{\left[x_c^{opt} - x_c^{ref}\right]^2 + \left[y_c^{opt} - y_c^{ref}\right]^2}}{\lambda} \tag{11}$$

and

$$\Delta = \left\{ \frac{L^{opt} - L^{ref}}{L^{ref}} \right\} \times 100 \tag{12}$$

where the apexes "opt" and "ref" mean retrieved and actual quantities, respectively. Moreover, (x_c, y_c) is the position of the barycenter of the scatterer and L is its radius.

3.1 Homogeneous Scatterers

The first experiment deals with the reconstruction of a single lossless dielectric cylinder (test case "*dielTM_dec8f.exp*") which is supposed to lie within a square region of side $30\,cm$. The object is located at $(x_c^{ref} = 0.0\,,\; x_c^{ref} = -30.0)\,mm$ and is characterized by a contrast value equal to $\tau(x,y) = 2.0 \pm 0.3$. Figure 1 shows the reconstructions of the object function of the bare approach (left column) and the $IMSA - NR$ (right column). Six different illumination frequencies in the range $[1;6]\,GHz$ with step $1\,GHz$ have been used. At each frequency, $V = 36$ different views have been considered and the data have been collected on $M^{(v)} = 49$ measurement points [24]. The side of the investigation domain expressed in wavelengths varies from one λ at the lowest frequency up to 6λ at the highest frequency. In each simulation, Γ_{inv} has been subdivided into $N = 400$ and $N(i) = 100$, $i = 1, ..., I$, cells for the bare and multi-resolution approach, respectively.

As it can be observed (Fig. 1), the values of the object functions retrieved with the $IMSA - NR$ method are much closer to the actual ones and, thanks the multi-scaling procedure, the scatterer is better localized within the investigation domain Γ_{inv} where the actual position of

the scatterer is indicated by the dashed line. This fact is further confirmed by the values of the error figures (11) and (12) in Fig. 2(*a*) and Fig. 2(*b*) pointing out that the $IMSA - NR$ solutions are definitely better than those retrieved with the bare procedure. Although some location errors (mainly in the high frequencies) for the $IMSA - NR$ are higher than those of the bare method [Fig. 2(*a*)], it should be noted that the corresponding occupation area errors of the bare procedure are one order of magnitude higher than those of the $IMSA - NR$ [Fig. 2(*b*)]. Consequently, although the position of the barycenter is better estimated by the bare method, the qualitative reconstructions turn out being worse as compared to the results of the $IMSA - NR$.

The reconstructions of the equivalent current densities for the experiments in Fig. 1 are given in Fig. 3. On one hand, it is worth noting that the solutions at the lower frequencies are better than those retrieved at higher frequencies. On the other hand, the $IMSA - NR$ approach always outperforms the bare procedure in terms of retrieved current distributions as well as absence of noise and artifacts in the background. As far as the minimization of Ψ is concerned, the value of the cost function at each iteration is reported in Fig. 4 for the data collected at $4\,GHz$, where $S_{end} = 4$. In the simulations, $K = 2000$ iterations are considered for the bare procedure and $K^{(s)} = 2000$ iterations are used at each step of the multi-resolution strategy, $i = 1, ..., I$. For the sake of completeness, some computational indexes for the results related to Fig. 4 are reported in Tab. I where U is the number of problem unknowns, K_{tot} is the total number of iterations, T_{tot} and T_k is the total CPU time and that required for a single iteration, respectively. The numerical simulations have been run on a $3\,GHz$ PC with $1\,GB$ of RAM.

In the second experiment, the data set "*twodielTM_8f.exp*" is taken into account. Two objects identical to that of the previous example are embedded within the region under test. The distance between the two barycenters is $d = 90\,mm$ and the data have been collected as for the first experiment. The reconstructed object functions obtained through the $IMSA - NR$ approach are shown in Fig. 5. The images are concerned with the inversions of the data at $f = [1, 2, 3, 4]\,GHz$. The best reconstruction from both a quantitative and qualitative point of view is achieved at $3\,GHz$ [Fig. 5(*c*)]. It is also interesting to notice that at lower frequencies the reconstructions are characterized by a low-pass behavior [Fig. 5(*a*)], while sharper edges

result at higher frequencies. Moreover, the distance between the barycenters is over-estimated at $f = 2\,GHz$ [Fig. 5(b)] and under-estimated at $f = 4\,GHz$ [Fig. 5(d)].

The reconstruction of a lossy target is performed in the third experiment (*"rectTM_cent.exp"*). The rectangular cylinder is located at the center of the investigation domain. It has been illuminated by a TM-polarized wave [24] at $f = 4\,GHz$. The dimensions of the scatterer in wavelengths turns out being equal to $0.17\lambda \times 0.34\lambda$. Figure 6 gives the reconstructions of the object function [Figs. 6(a)-(b)] and the equivalent current density [Figs. 6(c)-(d)] from the bare procedure [Figs. 6(a)-(c)] and the $IMSA - NR$ approach [Figs. 6(b)-(d)]. Although some artifacts are present in the background [see Figs. 6(b) and 6(d)], the enhancement in the reconstruction is non-negligible.

3.2 Inhomogeneous Scatterers

In this section, the reconstruction of inhomogeneous scatterers is dealt with. Two different experiments are taken into account, namely the data set "*FoamDielExtTM*" and "*FoamDielIntTM*" [25]. Two scatterers of radius $L_1 = 80\,mm$ and $L_2 = 30\,mm$ and contrast value equal to $\tau_1(x, y) = 0.45$ and $\tau_2(x, y) = 2.0$ are considered. In the first experiment, the objects are placed one close to the other (Fig. 7 - dashed line). In the second one, the smaller scatterer is located within the bigger one (Fig. 8 - dashed line). For each illumination frequency, $V = 8$ different views and the same number of measurement points as for the previous examples ($M^{(v)} = 49$) are used. Moreover, the dimension as well as the discretization of Γ_{inv} are set to those considered for homogeneous scatterers. As far as the test case "*FoamDielExtTM*" is concerned, the distributions of the object function retrieved by means of the bare procedure and the $IMSA - NR$ approach are compared in Fig. 7 where $f \in [2; 5]\,GHz$. Whatever the case, the two objects can be clearly distinguished both in terms of dimension as well as contrast function value when using the $IMSA - NR$. The same cannot be stated for the reconstructions with the bare approach. As a matter of fact, many artifacts are present in Fig. 7(a) and Fig. 7(e) when $f = 2\,GHz$ and $f = 4\,GHz$, respectively.

Finally, the $IMSA - NR$ approach is tested against the experimental data set "*FoamDielIntTM*" and the solutions obtained at the frequencies $f = [2, 3, 4, 5]\,GHz$ are given in Fig. 8. Although

the two objects can be identified in all the reconstructions, the scatterers are better localized and the best result is obtained when working at $4\,GHz$.

4 Conclusions

In this paper, the $IMSA - NR$ approach for the solution of inverse scattering problems has been validated against experimental data. The results have confirmed the effectiveness of the multi-resolution approach as compared to the single step method. In all the reported examples, the reconstructions of the $IMSA - NR$ resulted quite accurate both in terms of qualitative and quantitative imaging.

References

[1] M. Soleimani, "Simultaneous reconstruction of permeability and conductivity in magnetic induction tomography," *Journal of Electromagnetic Waves and Applications*, vol. 23, pp. 785-798, 2009.

[2] M. Goharian, M. Soleimani, and G. Moran, "A trust region subproblem for 3D electrical impedance tomography inverse problem using experimental data," *Progress In Electromagnetics Research*, vol. 94, pp. 19-32, 2009.

[3] M. Soleimani, C. N. Mitchell, R. Banasiak, R. Wajman, and A. Adler, A., "Four-dimensional electrical capacitance tomography imaging using experimental data," *Progress In Electromagnetics Research*, vol. 90, pp. 171-186, 2009.

[4] T. M. Habashy, E. Y. Chow, and D. G. Dudley, "Profile inversion using the renormalized source-type integral equation approach," *IEEE Trans. Antennas Propag.*, vol. 38, no. 5, pp. 668-681, May 1990.

[5] S. Caorsi, G. L. Gragnani, and M. Pastorino, "A multiview microwave imaging system for two-dimensional penetrable objects," *IEEE Trans. Microw. Theory Tech.*, vol. 39, no. 5, pp. 845-851, May 1991.

[6] T. M. Habashy, M. L. Oristaglio, and A. T. de Hoop, "Simultaneous nonlinear reconstruction of two-dimensional permittivity and conductivity," *Radio Science*, vol. 29, no. 4, pp. 1101-1118, 1994.

[7] S. Caorsi, and G. L. Gragnani, "Inverse-scattering method for dielectric objects based on the reconstruction of the nonmeasurable equivalent current density," *Radio Science*, vol. 34, no. 1, pp. 1-8, 1999.

[8] K. Persson and M. Gustafsson, "Reconstruction of equivalent currents using a near-field data transformation with radome applications," *Progress In Electromagnetics Research*, vol. 54, pp. 179-198, 2005.

[9] M. Khalaj-Amirhosseini, "Analysis of lossy inhomogeneous planar layers using equivalent sources method," *Progress In Electromagnetics Research*, vol. 72, pp. 61-73, 2007.

[10] R. Alaia, D. Patella, and P. Mauriello, "Imaging multipole self-potential sources by 3D probability tomography," *Progress In Electromagnetics Research B*, vol. 14, pp. 311-339, 2009.

[11] J. Hadamard, *Lectures on the Cauchy Problem in Linear Partial Differential Equations*. New Haven, CT: Yale Univ. Press, 1923.

[12] A. J. Devaney and E. Wolf, "Radiating and nonradiating classical current distributions and the fields they generate," *Phys. Rev. D Part. Fields*, vol. 8, no. 4, pp. 1044-1047, Aug. 1973.

[13] N. Bleistein and J. K. Cohen, "Nonuniqueness in the inverse source problem in acoustics and electromagnetics," *J. Math. Phys. N. Y.*, vol. 18, no. 2, pp. 194-201, Feb. 1977.

[14] W. C. Chew, Y. M. Wang, G. Otto, D. Lesselier and J. C. Bolomey, "On the inverse source method of solving inverse scattering problems," *Inverse Problems*, vol. 10, pp. 547-553, 1994.

[15] D. G. Dudley, T. M. Habashy and E. Wolf, "Linear inverse problems in wave motion: Nonsymmetric first-kind integral equations," *IEEE Trans. Antennas Propag.*, vol. 48, no. 10, pp. 1607-1617, Oct. 2000.

[16] E. A. Marengo and R. W. Ziolkowski, "Nonradiating and minimum energy source and their fields: Generalized source inversion theory and applications," *IEEE Trans. Antennas Propag.*, vol. 48, no. 10, pp. 1553-1562, Oct. 2000.

[17] M. M. Ney, A. M. Smith, and S. S. Stuchly, "A solution of electromagnetic imaging using pseudoinverse transformation," *IEEE Trans. Med. Imag.*, vol. 3, no. 4, pp. 155-162, 1984.

[18] O. M. Bucci and T. Isernia, "Electromagnetic inverse scattering: Retrievable information and measurements strategies," *Radio Science*, vol. 32, no. 6, pp. 2123-2138, 1997.

[19] P. Rocca, M Donelli, G. L. Gragnani, and A Massa, "Iterative multi-resolution retrieval of non-measurable equivalent currents for the imaging of dielectric objects," *Inverse Problems*, vol. 25, pp. 1-15, 2009.

[20] S. Caorsi, M. Donelli, D. Franceschini and A. Massa, "A new methodology based on an iterative multiscaling for microwave imaging," *IEEE Trans. Microw. Theory Tech.*, vol. 51, no. 4, pp. 1162-1173, Apr. 2003.

[21] S Caorsi, M. Donelli, and A. Massa, "Detection, location, and imaging of multiple scatterers by means of the iterative multiscaling method," *IEEE Trans. Microw. Theory Tech.*, vol. 52, no. 4, pp. 1217-1228, Apr. 2004.

[22] D. Colton and R. Krees, *Inverse Acoustics and Electromagnetic Scattering Theory*. Berlin, Germany: Springer-Verlag, 1992.

[23] R. E. Kleinmann and P. M. Van den Berg, "A modified gradient method for two-dimensional problems in tomography," *J. Comput. Appl. Math.*, vol. 42, no. 1, pp. 17-35, 1992.

[24] K. Belkebir and M. Saillard, "Testing inversion algorithms against experimental data," *Inverse Problems*, vol. 17, no. 6, pp. 1565-1571, Dec. 2001.

[25] K. Belkebir and M. Saillard, "Testing inversion algorithms against experimental data: inhomogeneous data," *Inverse Problems*, vol. 21, no. 6, pp. 1-3, Dec. 2005.

[26] A. Semnani and M. K. Hesari, "Truncated cosine fourier series expansion method for solving 2-D inverse scattering problems," *Progress In Electromagnetics Research*, vol. 81, pp. 73-97, 2008.

FIGURE CAPTIONS

- **Figure 1.** *Dataset "dielTM_dec8f.exp" - Benchmark "Marseille"* [24]. *Object Function Reconstruction* - Retrieved distributions with the "bare" procedure (*left*) and the $IMSA-NR$ approach at $s = S_{end}$ (*right*). Working frequency: (*a*)(*b*) $f = 1\,GHz$, (*c*)(*d*) $f = 2\,GHz$, (*e*)(*f*) $f = 3\,GHz$, (*g*)(*h*) $f = 4\,GHz$, (*i*)(*l*) $f = 5\,GHz$, (*m*)(*n*) $f = 6\,GHz$.

- **Figure 2.** *Dataset "dielTM_dec8f.exp" - Benchmark "Marseille"* [24]. Qualitative error figures for the reconstructions of Fig. 1: (*a*) location error δ and (*b*) occupation area error Δ.

- **Figure 3.** *Dataset "dielTM_dec8f.exp" - Benchmark "Marseille"* [24]. *Equivalent Current Density Reconstruction* - Retrieved distributions with the "bare" procedure (*left*) and the $IMSA-NR$ approach at $s = S_{end}$ (*right*). Working frequency: (*a*)(*d*) $f = 1\,GHz$, (*b*)(*e*) $f = 2\,GHz$, (*c*)(*f*) $f = 3\,GHz$, (*g*)(*l*) $f = 4\,GHz$, (*h*)(*m*) $f = 5\,GHz$, (*i*)(*n*) $f = 6\,GHz$.

- **Figure 4.** *Dataset "dielTM_dec8f.exp" - Benchmark "Marseille"* [24] ($f = 4\,GHz$) - Behavior of the cost function value for the "bare" procedure and the $IMSA-NR$ approach.

- **Figure 5.** *Dataset "twodielTM_8f.exp" - Benchmark "Marseille"* [24]. *Object Function Reconstruction* - Retrieved distributions with the $IMSA-NR$ approach at $s = S_{end}$. Working frequency: (*a*) $f = 1\,GHz$, (*b*) $f = 2\,GHz$, (*c*) $f = 3\,GHz$, (*d*) $f = 4\,GHz$.

- **Figure 6.** *Dataset "rectTM_cent.exp" - Benchmark "Marseille"* [24] ($f = 4\,GHz$) - Reconstruction of (*a*)(*b*) the object function and of (*c*)(*d*) the equivalent current density retrieved with (*a*)(*c*) the "bare" procedure and (*b*)(*d*) the $IMSA-NR$ approach.

- **Figure 7.** *Dataset "FoamDielExtTM" - Benchmark "Marseille"* [25]. *Object Function Reconstruction* - Retrieved distributions with the "bare" procedure (*left*) and the $IMSA-NR$ approach at $s = S_{end}$ (*right*). Working frequency: (*a*)(*b*) $f = 2\,GHz$, (*c*)(*d*) $f = 3\,GHz$, (*e*)(*f*) $f = 4\,GHz$, (*g*)(*h*) $f = 5\,GHz$.

- **Figure 8.** *Dataset "FoamDielIntTM" - Benchmark "Marseille"* [25]. *Object Function Reconstruction* - Retrieved distributions with the $IMSA - NR$ approach at $s = S_{end}$. Working frequency: (*a*) $f = 2\,GHz$, (*b*) $f = 3\,GHz$, (*c*) $f = 4\,GHz$, (*d*) $f = 5\,GHz$.

TABLE CAPTIONS

- **Table 1.** *Dataset "dielTM_dec8f.exp" - Benchmark "Marseille"* [24] ($f = 4\,GHz$). *Computational Issues* - Values of the computational indexes in correspondence with the bare procedure and the $IMSA - NR$ approach.

(a)

2.3 $Re\left\{\tau\left(x,y\right)\right\}$ 0.0

(b)

2.3 $Re\left\{\tau\left(x,y\right)\right\}$ 0.0

(c)

2.3 $Re\left\{\tau\left(x,y\right)\right\}$ 0.0

(d)

2.3 $Re\left\{\tau\left(x,y\right)\right\}$ 0.0

(e)

2.3 $Re\left\{\tau\left(x,y\right)\right\}$ 0.0

(f)
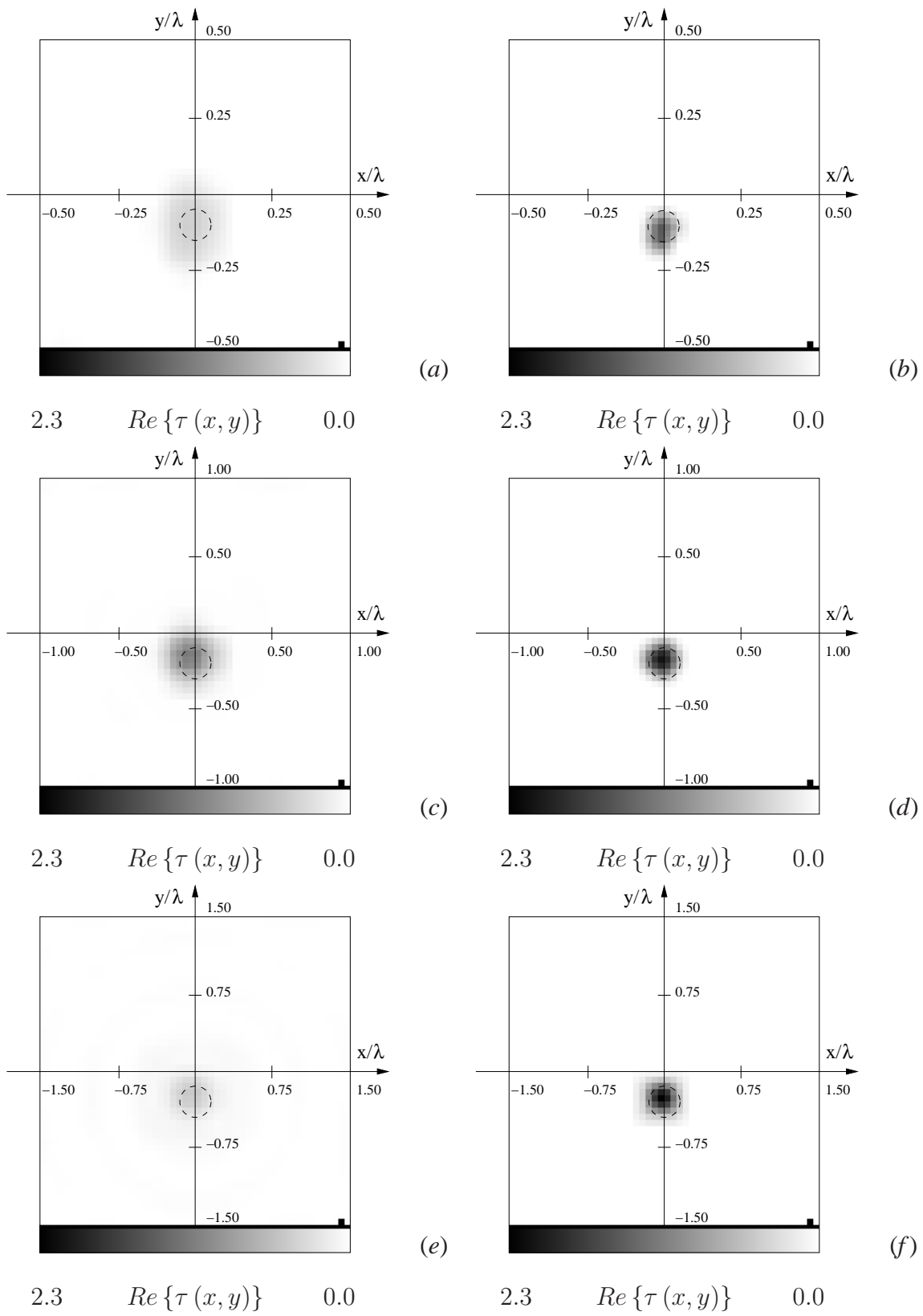
2.3 $Re\left\{\tau\left(x,y\right)\right\}$ 0.0

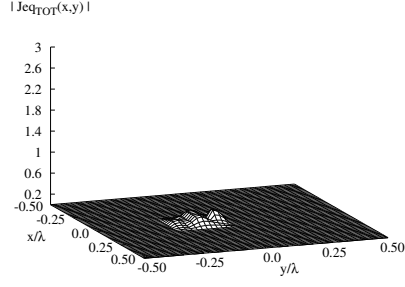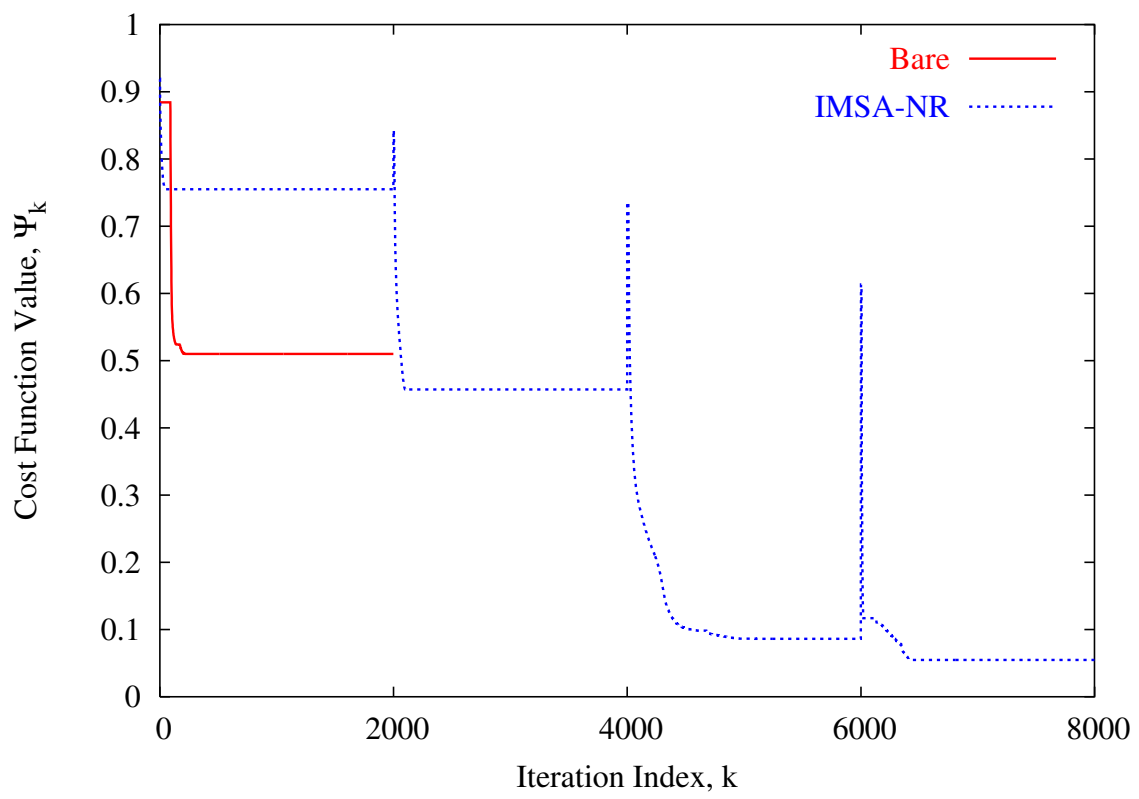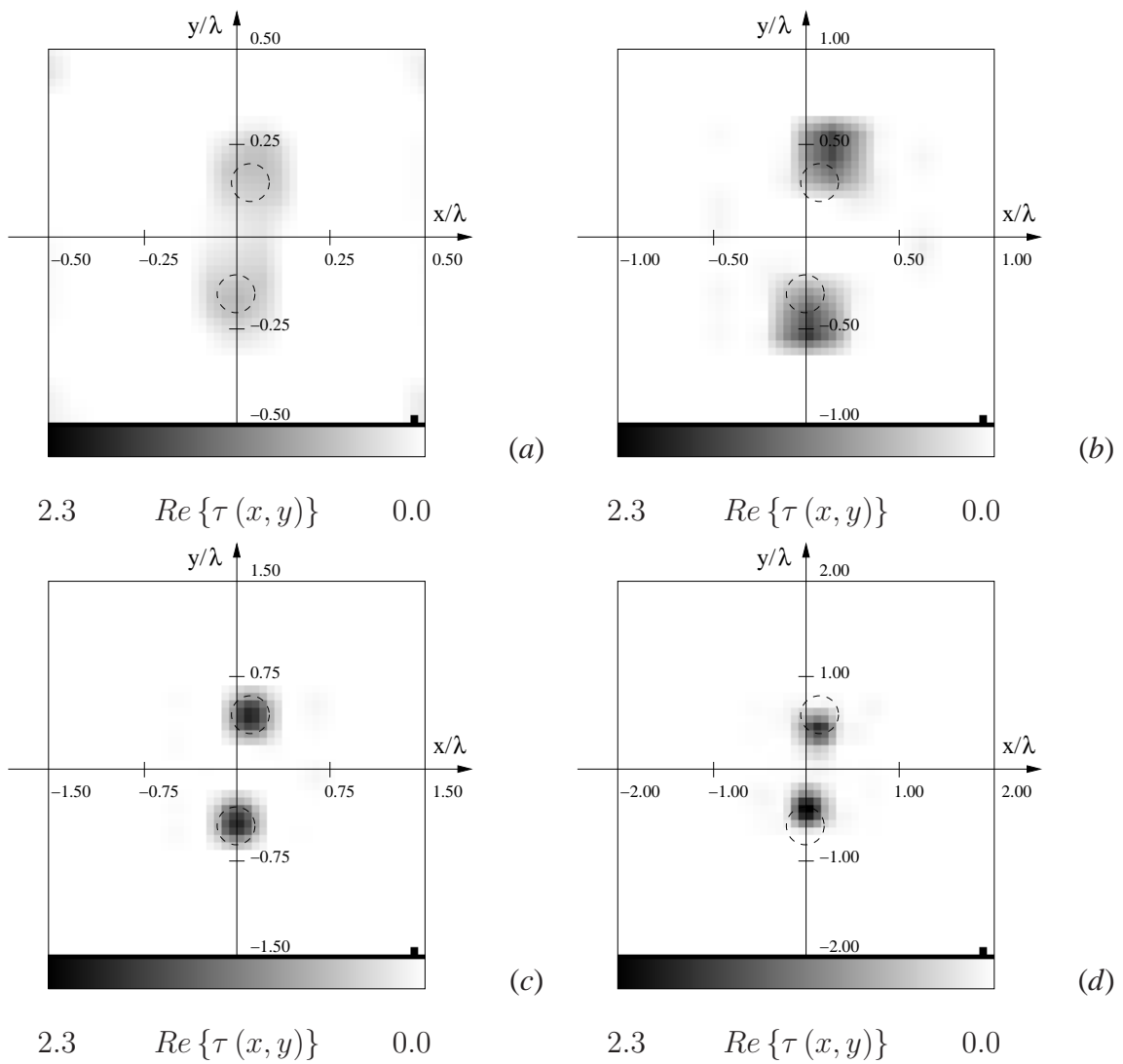**Fig. 1(*I*) - P. Rocca,** "Multi-resolution Retrieval of Non-measurable Equivalent Currents ..."

(g)

2.3 $\qquad Re\{\tau(x,y)\}$ 0.0

(h)

2.3 $\qquad Re\{\tau(x,y)\}$ 0.0

(i)

2.3 $\qquad Re\{\tau(x,y)\}$ 0.0

(l)

2.3 $\qquad Re\{\tau(x,y)\}$ 0.0

(m)
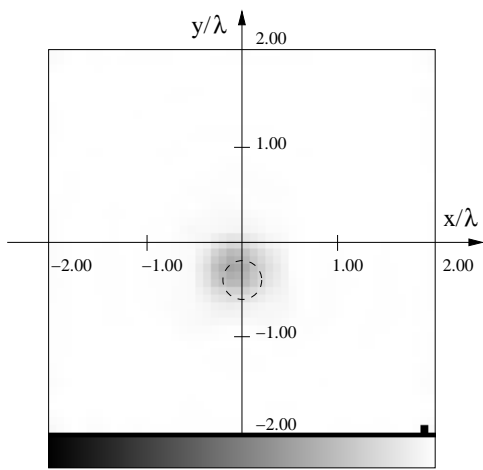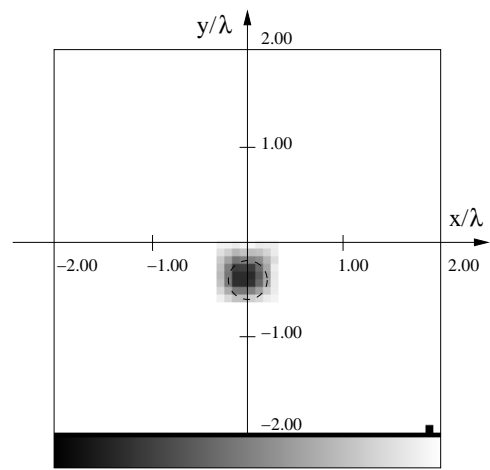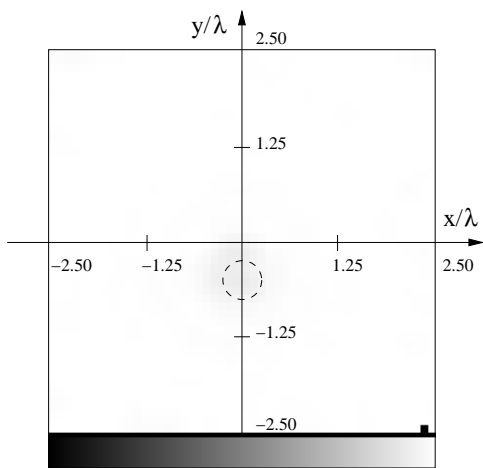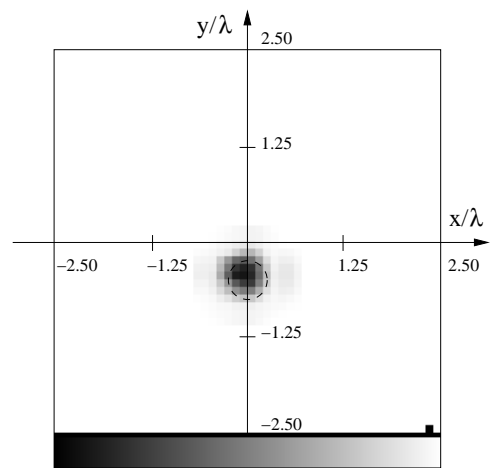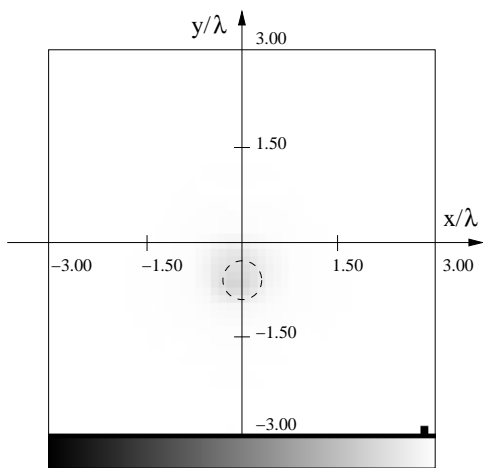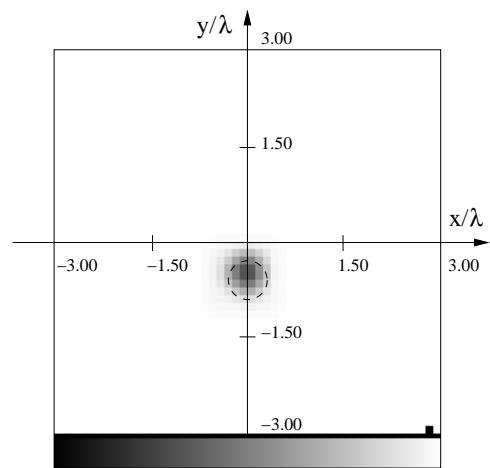
2.3 $\qquad Re\{\tau(x,y)\}$ 0.0

(n)

2.3 $\qquad Re\{\tau(x,y)\}$ 0.0

Fig. 1(*II*) - P. Rocca, "Multi-resolution Retrieval of Non-measurable Equivalent Currents ..."
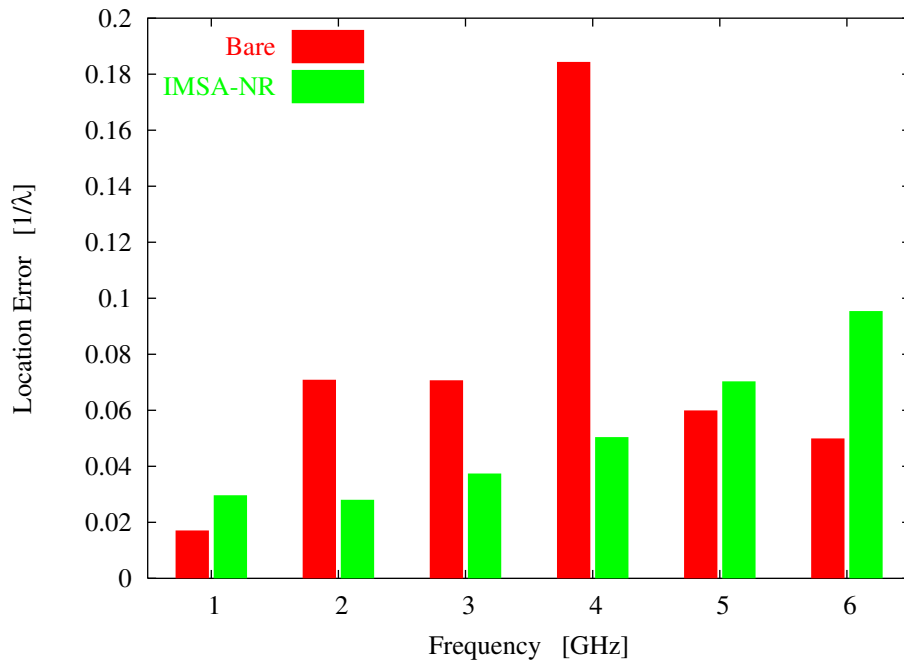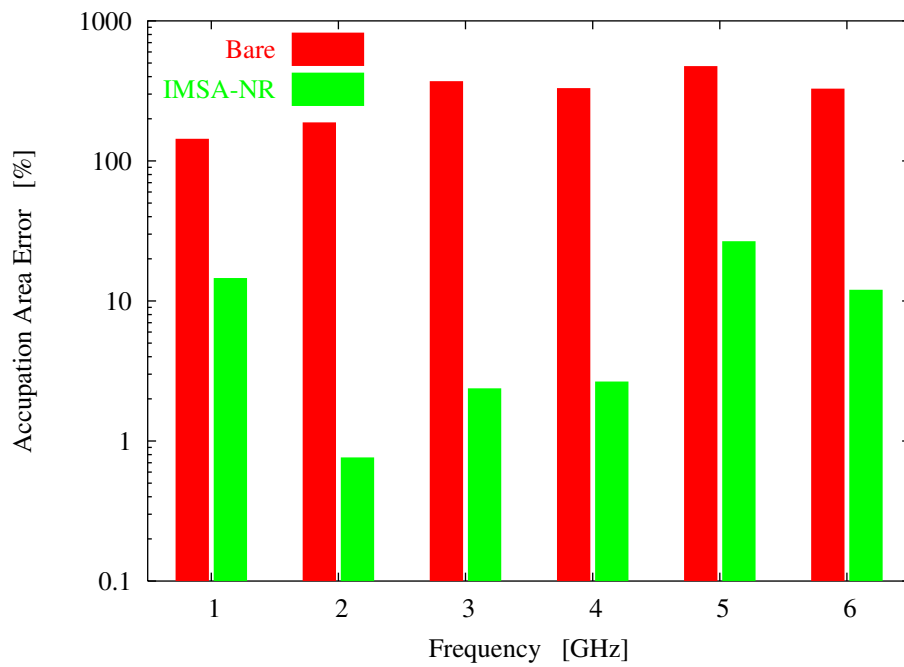
(a)

(b)
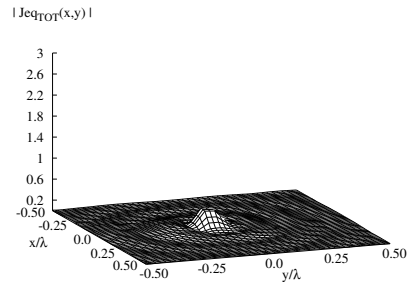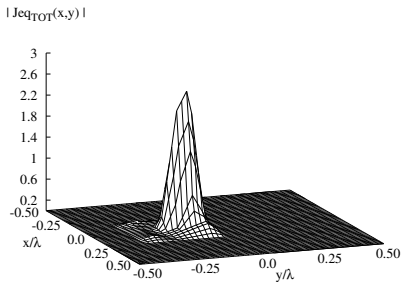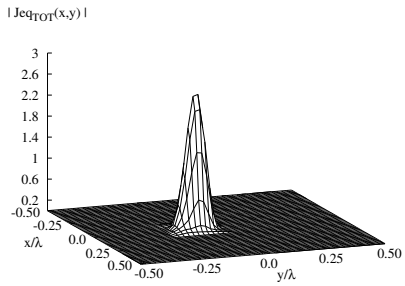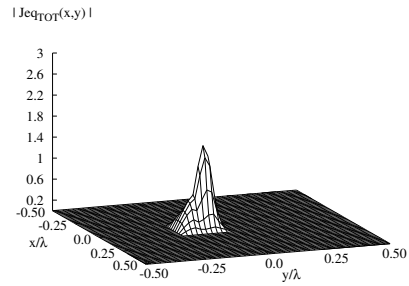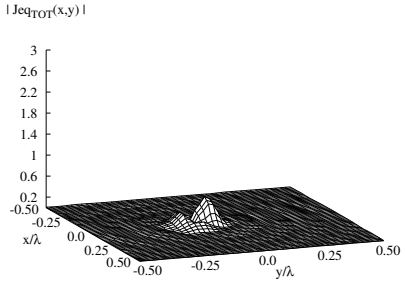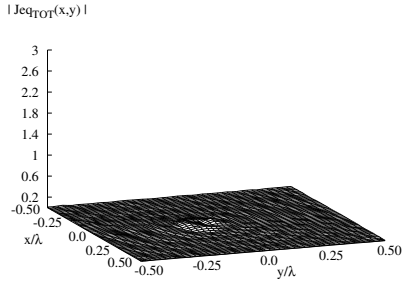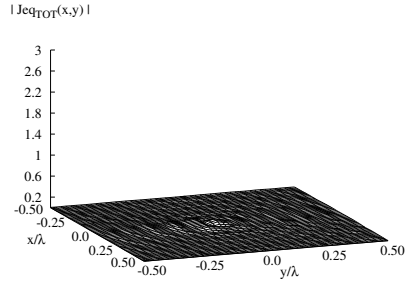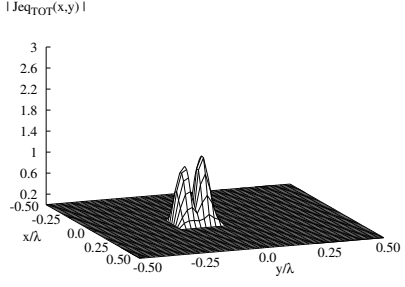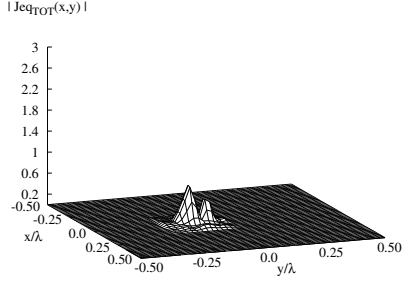
Fig. 2 - P. Rocca, "Multi-resolution Retrieval of Non-measurable Equivalent Currents ..."

Fig. 3(*I*) - P. Rocca, "Multi-resolution Retrieval of Non-measurable Equivalent Currents ..."

Fig. 3(II) - P. Rocca, "Multi-resolution Retrieval of Non-measurable Equivalent Currents ..."
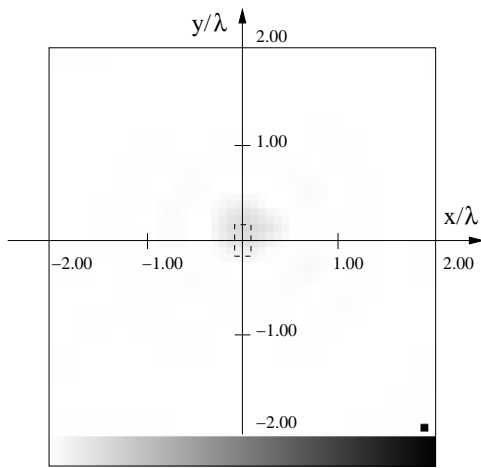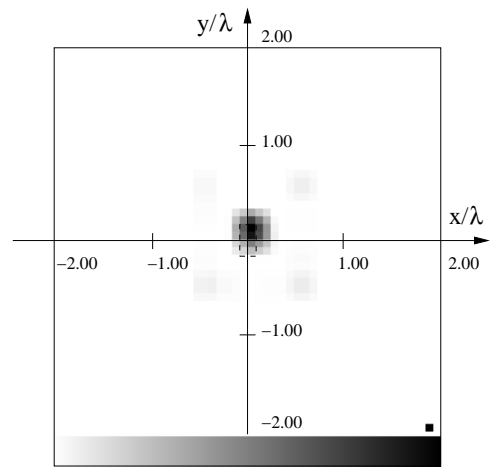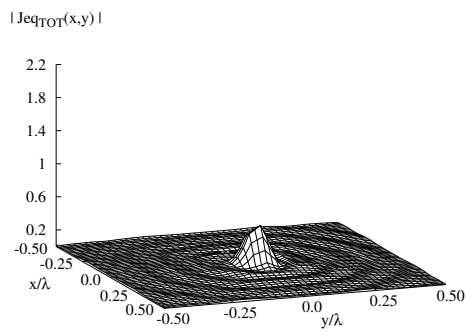
Fig. 4 - P. Rocca, "Multi-resolution Retrieval of Non-measurable Equivalent Currents ..."

(a)

2.3 $Re\{\tau(x,y)\}$ 0.0

(b)

2.3 $Re\{\tau(x,y)\}$ 0.0

(c)

2.3 $Re\{\tau(x,y)\}$ 0.0

(d)

2.3 $Re\{\tau(x,y)\}$ 0.0

Fig. 5 - P. Rocca, "Multi-resolution Retrieval of Non-measurable Equivalent Currents ..."

22

(a)
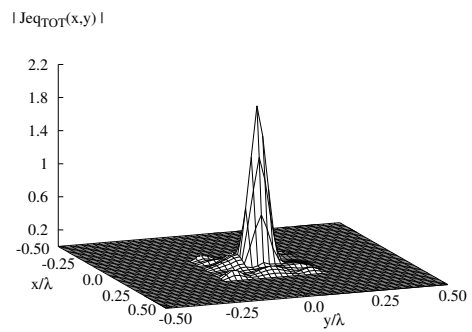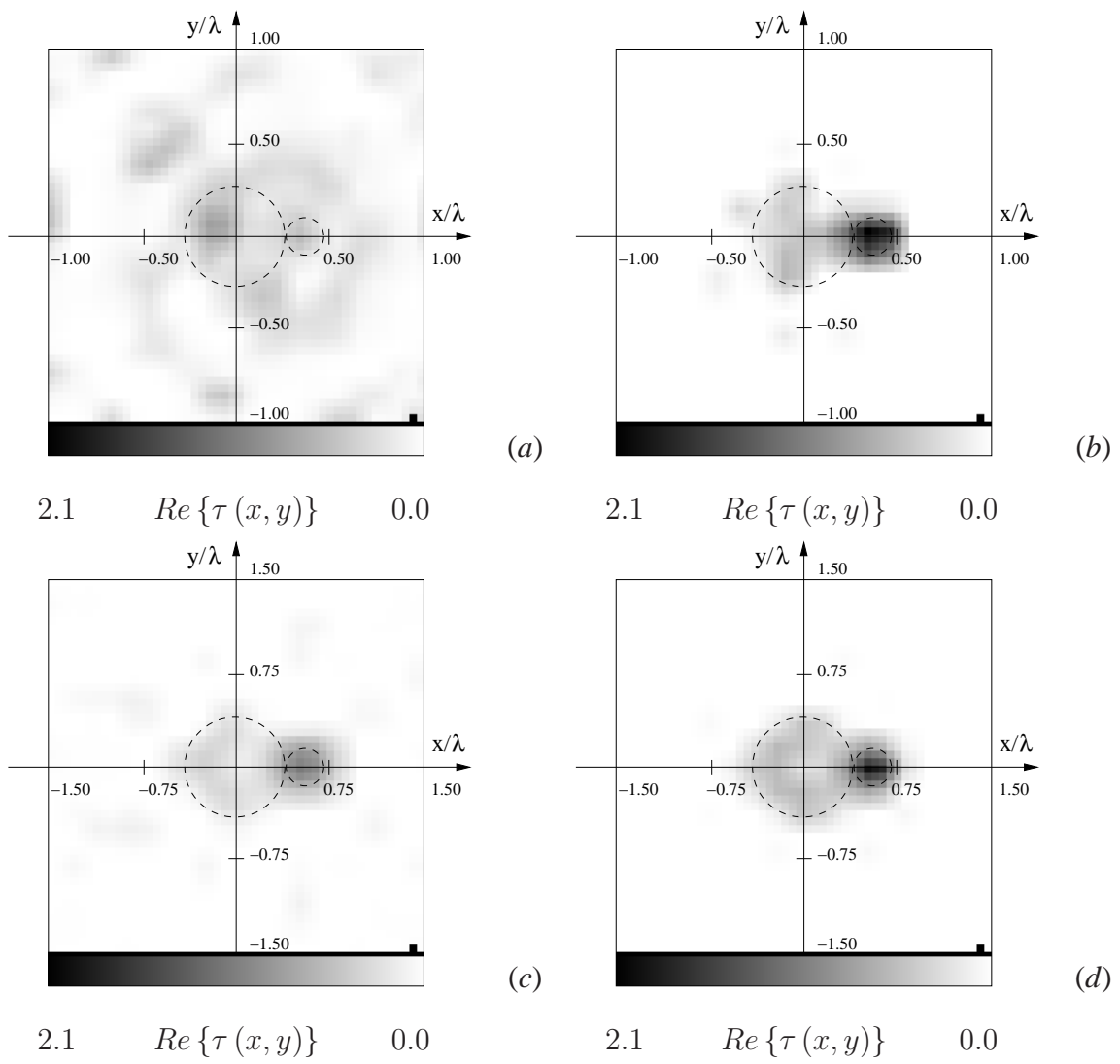
(b)

(c)

(d)

Fig. 6 - P. Rocca, "Multi-resolution Retrieval of Non-measurable Equivalent Currents ..."

(a)

2.1 $\quad Re\{\tau(x,y)\} \quad$ 0.0

(b)

2.1 $\quad Re\{\tau(x,y)\} \quad$ 0.0

(c)

2.1 $\quad Re\{\tau(x,y)\} \quad$ 0.0
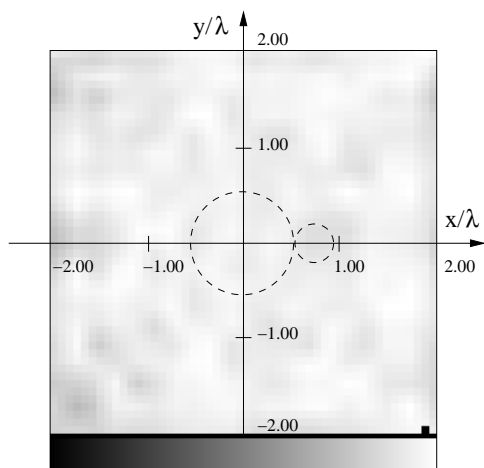
(d)

2.1 $\quad Re\{\tau(x,y)\} \quad$ 0.0

Fig. 7(*I*) - P. Rocca, "Multi-resolution Retrieval of Non-measurable Equivalent Currents ..."

24

(e)

2.1 $Re\left\{\tau\left(x,y\right)\right\}$ 0.0

(f)

2.1 $Re\left\{\tau\left(x,y\right)\right\}$ 0.0

(g)

2.1 $Re\left\{\tau\left(x,y\right)\right\}$ 0.0

(h)
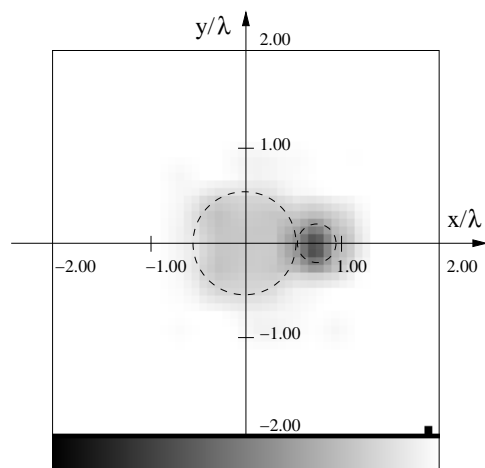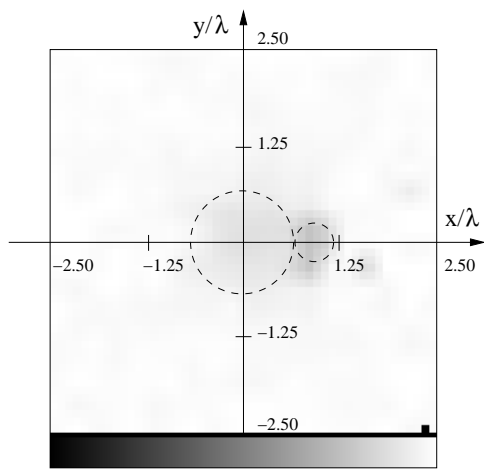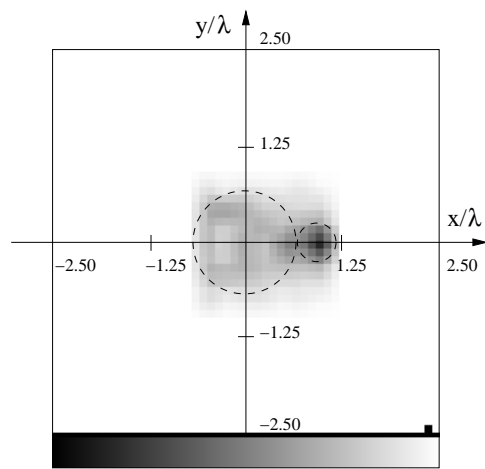
2.1 $Re\left\{\tau\left(x,y\right)\right\}$ 0.0

Fig. 7(*II*) - P. Rocca, "Multi-resolution Retrieval of Non-measurable Equivalent Currents ..."

(a)

2.1 $Re\left\{\tau\left(x,y\right)\right\}$ 0.0

(b)

2.1 $Re\left\{\tau\left(x,y\right)\right\}$ 0.0

(c)

2.1 $Re\left\{\tau\left(x,y\right)\right\}$ 0.0

(d)

2.1 $Re\left\{\tau\left(x,y\right)\right\}$ 0.0
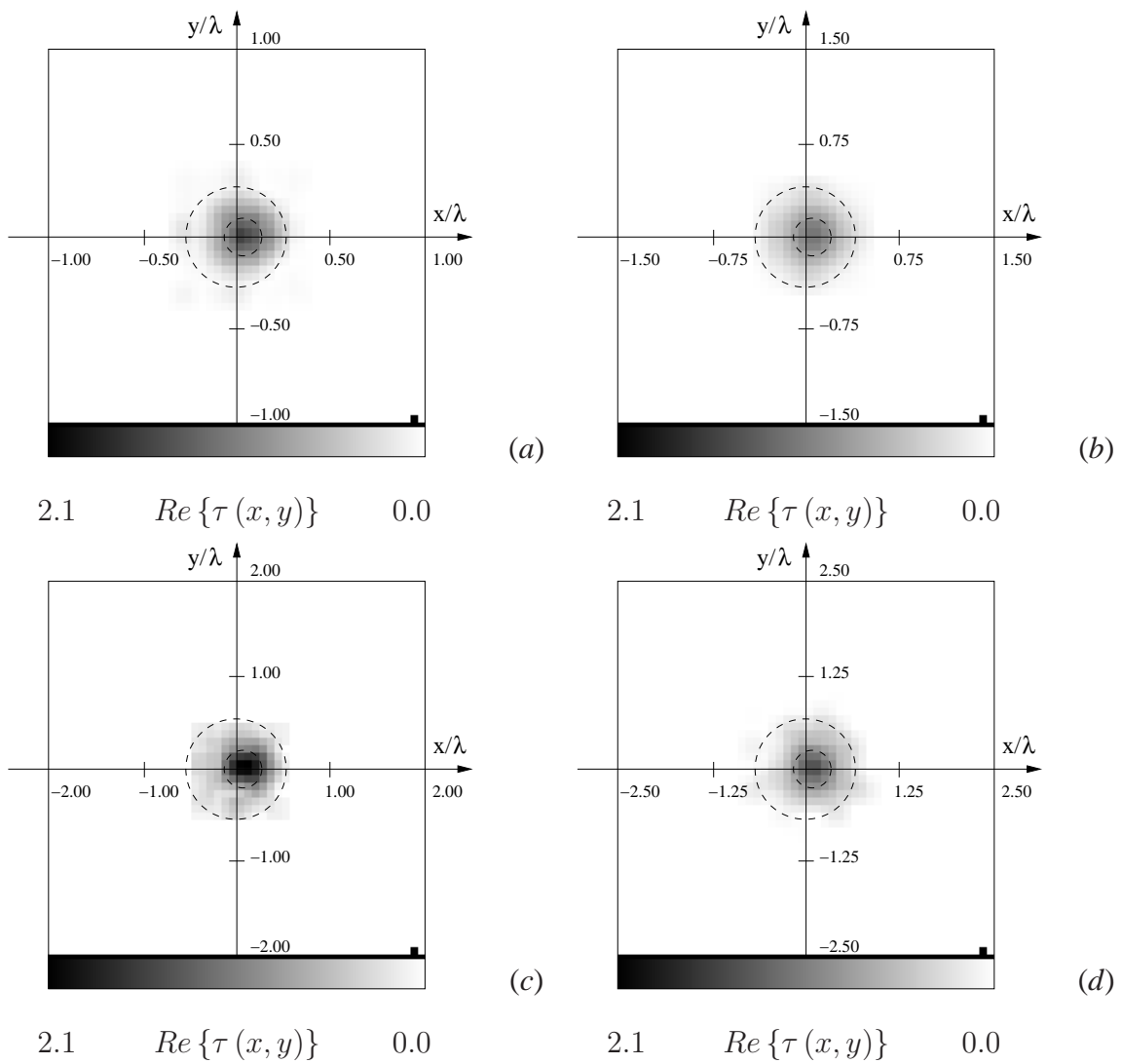
Fig. 8 - P. Rocca, "Multi-resolution Retrieval of Non-measurable Equivalent Currents ..."

	$Bare$	$IMSA-NR$
U	2.96×10^4	7.4×10^3
K_{tot}	2000	8000
S_{end}	$-$	4
$T_k\,[sec]$	6.08×10^{-1}	2.64×10^{-2}
$T_{tot}\,[sec]$	1224.3	214.4

Tab. I - P. Rocca, "Multi-resolution Retrieval of Non-measurable Equivalent Currents ..."